Unexpectedly large intra-grain crystal rotations in CVD-grown (Ti,Al)N coatings and their relation to internal nanolamella structures

Materials & Design 266 (2026) 116146

Contents lists available at ScienceDirect

Materials & Design

journal homepage: www.elsevier.com/locate/matdes

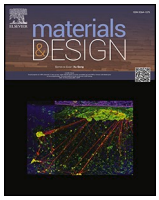

Unexpectedly large intra-grain crystal rotations in CVD-grown (Ti,Al)N coatings and their relation to internal nanolamella structures

Ren Qiu [a,*], Olof Bäcke [a,b], Dirk Stiens [b], Hans-Olof Andrén [a], Mats Halvarsson [a,*]

[a] Department of Physics, Chalmers University of Technology, SE-412 96 Gothenburg, Sweden
[b] Walter AG, D-72072 Tübingen, Germany

A B S T R A C T

The crystal growth direction within a single grain is typically assumed to be uniform. However, this study presents the first observation of spontaneous intra-grain crystal rotations in (Ti,Al)N grains with an internal nanolamella structure. The rotation occurs spontaneously during grain growth in a chemical vapor deposition process. The crystal rotations exhibit a highly symmetrical pattern linked to the (Ti,Al)N grain morphology: a pyramid comprising three {001}-faceted domains. The crystal lattices systematically rotate within each domain toward the pyramid tip, with the largest rotations concentrated at the pyramid edges. Within a single (Ti,Al)N grain, the crystal orientation can shift up to 15° from base to tip, with a typical gradient of 1°/μm. The rotation gradient reaches a peak of 3 – 4°/μm in the horizontal direction near the pyramid edges. This phenomenon is attributed to the high density of grown-in dislocations, arising from interface mismatches between the (Ti,Al)N grain domains and hexagonal AlN nano-precipitates that form at the domain boundaries. Analysis of three (Ti,Al)N samples with varying nanolamella structures reveals that the presence of more nanolamellae corresponds to larger crystal rotations. These findings provide useful insights into controlling crystal rotation and its potential influence on material properties, opening new avenues for materials design and optimization.

1. Introduction

Hard ceramic coatings, particularly transition metal nitrides, carbide and oxides, are widely used in cutting tools to enhance wear-resistance under extreme thermal and mechanical loads during high-speed metal machining [1]. Chemical vapor deposition (CVD) is a commonly employed technique for synthesizing these coatings, typically resulting in polycrystalline films with a strong fibre texture. The formation of such texture is conventionally explained by the competitive growth mode proposed by van der Drift in 1960 s [2,3], where grains with the fastest-growing crystallographic orientations dominate the microstructure.

Research has shown that specific fiber textures can improve the wear resistance of coatings at high temperatures, and the most favorable texture direction depends on the crystal structure of the coating material [4–7]. This is related to the orientations of the grains relative to external forces and the resulting grain deformation under the machining condition. For instance, CVD process parameters have been adjusted to obtain different fiber textures in Ti(C,N) and κ-Al_2O_3 coatings for optimizing their wear-resistance [4–10]. The texture-dependent wear resistance suggests that tuning the crystal growth orientations can provide new ways to modify the mechanical properties of coatings. In addition, titanium aluminum nitride (denoted as (Ti,Al)N) coatings have been grown with different fiber textures by physical and chemical vapor deposition (PVD and CVD), where a correlation between texture and coating residual stress was reported [1112].

While previous studies focus on the variation of growth directions between grains and texture evolution in the CVD coatings [2,3,11,12], little attention has been given to the possibility of intra-grain crystal rotations during growth, and their potential impact on the mechanical properties of coatings has not yet been explored.

It is traditionally assumed that once the orientation of a grain is established during nucleation it remains unchanged during growth, unless external stresses or plastic deformations are introduced. However, recent studies on one-dimensional (1D) nanostructures have demonstrated that spontaneous crystal rotation can occur even in the absence of external forces. In nanowires such as PbS [13], PbSe [14], ZnO [15], InP [16], and GeS [17,18], an Eshelby twist (ref. [19]) mechanism has been shown to induce continuous axial rotation via screw components of a grown-in dislocations. The Eshelby twist has also been reported in ZnO nanotubes [20] and carbon nanotubes [21]. These findings raise the question of whether a similar growth-induced crystal rotation phenomenon could also take place in three-dimensional (3D) grains.

In this study, we report the first direct observations of spontaneous crystal rotations within individual (Ti,Al)N grains during CVD growth of polycrystalline films. Using detailed electron backscattered diffraction

* Corresponding authors.
E-mail addresses: renqiu.helsinki@outlook.com (R. Qiu), mats.halvarsson@chalmers.se (M. Halvarsson).

https://doi.org/10.1016/j.matdes.2026.116146
Received 25 January 2026; Received in revised form 20 April 2026; Accepted 28 April 2026
Available online 29 April 2026

(EBSD) in scanning electron microscopy (SEM) and complementary transmission electron microscopy (TEM), correlations between crystal rotation, the (Ti,Al)N grain morphology and internal nanolamella structure, and grown-in dislocations are revealed.

2. Experimental methods

2.1. CVD synthesis of (Ti,Al)N coatings

The (Ti,Al)N coatings are deposited using low-pressure CVD (LPCVD) on cemented carbide substrates (94 wt% tungsten carbide and 6 wt% cobalt). Deposition is conducted in an industrial-scale cylindrical hot-wall CVD reactor. Reactive precursors and carrier gases are introduced through a central inlet pipe, while reacted gases are evacuated through peripheral outlets. Details of the reactor setup can be found in previous papers and patents [22–26].

Prior to (Ti,Al)N deposition, a thin (less than 1 μm) TiN interlayer is first deposited to enhance adhesion between the (Ti,Al)N coating and the substrate. This TiN layer is deposited at 850 °C and 150 mbar using $TiCl_4$, N_2 and H_2 as precursors. Subsequently, the (Ti,Al)N coatings are deposited with $AlCl_3$, $TiCl_4$, NH_3 and H_2 as precursors. The deposition temperature is 725 °C, and the pressure is 8 mbar. Different setups are used for charging the samples inside the reactor, and the three samples are deposited using different reactive gas concentrations to adapt to the geometry and surface area inside the reactor. Table 1 gives an overview of the experimental conditions used for the (Ti,Al)N deposition. To achieve the internal nanolamella structure, a rotational precursor gas supply mechanism is employed, where the rotation frequency and local coating growth rate jointly determine the nanolamella periodicity, as reported in earlier studies [22]. The average [Ti]/[Al] ratio of the (Ti,Al)N coatings is close to 20/80, as has been reported in previous studies [22–24,26].

To investigate the effect of nanolamella periodicity on crystal rotation, three types of (Ti,Al)N samples were prepared: two with nanolamella structures, with periodicities of approximately 15 nm (sample 1) and 35 nm (sample 2), and one without a nanolamella structure (sample 3) deposited without gas inlet rotation [29]. For sample 1, an additional thin (less than 500 nm) TiN layer is deposited on top of the (Ti,Al)N at 850 °C using $TiCl_4$, NH_3, N_2 and H_2 as precursors. However, only the (Ti,Al)N layer is analyzed by EBSD and TEM in this work.

2.2. Microstructural characterization

TEM and scanning TEM (STEM) experiments were conducted using an FEI Titan 80–300 TEM/STEM instrument equipped with a Schottky field emission gun and a C_s-probe corrector. Thin foil samples for TEM/STEM characterization were prepared using an FEI Versa 3D focused ion beam-scanning electron microscope (FIB-SEM). Annular dark field (ADF) imaging and high-angle ADF (HAADF) imaging in STEM mode were performed using ADF and HAADF detectors. Selected area electron diffraction (SAED) and nanobeam electron diffraction (NBED) were applied for identifying phases and crystal orientations.

The EBSD experiments were conducted using a TESCAN GAIA3 FIB-SEM instrument equipped with an Oxford NanoNordlys detector. The SEM part of the instrument was operated at an accelerating voltage of 20 kV and an electron beam current of 1.5nA. Cross-sectional EBSD was performed on coating cross-sections polished using the FIB part. Plan-view thin-foil samples for EBSD analysis were prepared on the coating cross-section using the standard FIB-SEM lift-out method. While typical lift-out samples for TEM characterization have a thickness of approximately 100 nm, those used for EBSD in this work were polished to a thickness of 250–350 nm. This adjustment was made to avoid residual stress-induced bending, which would affect the EBSD results. Due to the greater thickness of these samples, transmission Kikuchi diffraction (TKD) is not feasible. Instead, orientation maps were obtained using the reflective EBSD mode. For those measurements, the lift-out samples were mounted on an Oxford Instruments TKD/EBSD holder and tilted at the standard 70° angle relative to the electron beam. The step size of EBSD map was 30 nm for both the cross-sectional and plan-view-sectional measurements. The EBSD data was subjected to a typical smoothing processing using the Oxford HKL Channel 5 software, and then analyzed by MTEX, an open source MATLAB toolbox for crystallographic texture analysis [27].

Table 1
Experimental conditions used for the (Ti,Al)N coating deposition.

Sample	#1	#2	#3
Gas rotation speed ν [1/min]	6	0.5	0
Nanolamella periodicity λ [nm]	15	35	0
(Ti,Al)N coating thickness [μm]	17	6	15
(Ti,Al)N deposition time [min]	153	260	75
(Ti,Al)N deposition temperature [°C]	725	725	725
(Ti,Al)N deposition pressure [mbar]	8	8	8

3. Results and discussion

3.1. Pyramidal morphology of the (Ti,Al)N grains and co-grown h-AlN

The (Ti,Al)N coating textures and grain morphologies are determined by competitive growth during the CVD process [3,12,22,25]. As the deposition progresses, grains generally tend to align their fastest-growing crystallographic orientations perpendicular to the substrate, in this case resulting in a 111 fiber texture. Simultaneously, {001} facet domains develop in each (Ti,Al)N grain, forming a pyramidal shape, which has a three-fold symmetry around the global growth direction along [111], as illustrated in Fig. 1 (a) [22,25].

To better visualize the relationship between crystallographic orientations and the pyramidal morphology, a Qiu-Halvarsson (Q-H) pyramid (named after two authors of this work, Ren Qiu and Mats Halvarsson) is introduced, as depicted in Fig. 1 (b) and (c). Unlike the conventional Thompson tetrahedron [28], which consists of four {111} planes and is commonly used for analyzing face centered cubic (FCC) metals, the Q-H pyramid consists of three {001} planes (ADB, ADC and BDC) and the (111) plane (ABC). In this pyramid, point δ represents the center of the ABC (111) plane, while points α, β, and γ correspond to the midpoints of edges BC, CA and AB, respectively. The three domains beneath the {001} planes (referred to as {001}-faceted domains) are projected onto the (111) plane as regions AδB, BδC, and CδA. The boundaries between these domains, δDA ($\bar{1}$ 10), δDB (10 $\bar{1}$) and δDC (0 $\bar{1}$ 1), are projected onto the (111) plane as lines δA, δB and δC.

A distinct internal nanolamella structure, with periodic alternations of Ti-rich (referred to as Ti(Al)N) and Al-rich (referred to as Al(Ti)N) sublayers along the (001) planes, is observed within the (Ti,Al)N grains. This structure, with a certain periodicity (λ), results from the rotational precursor gas supply during deposition. Fig. 2 (a) illustrates nanolamellae in sample 1 (λ = 15 nm), viewed along the [001] direction. More details of the nanolamella structure have been studied in previous studies [22,24–26].

For a (Ti,Al)N grain with its [111] direction aligned with the coating growth direction, a plan-view section of it corresponds to the ABC (111) plane of the Q-H pyramid. Fig. 2 (b) presents a plan-view sectional STEM HAADF micrograph of a (Ti,Al)N grain (sample 1, λ = 15 nm), where the Q-H pyramid framework is used to indicate local crystal orientations. Since the grain grows via a layer-by-layer epitaxy of the three {001} facets, the growth sequence within the plan-view section can be inferred. The intersections between the {001} facets and the (111) plane form along the [0 $\bar{1}$ 1] (AB), [$\bar{1}$ 10] (BC) and [10 $\bar{1}$] (CA) directions. Therefore, in each domain on the plan view section (ABδ, BCδ, or CAδ) features on a line along these intersection directions are deposited simultaneously. In addition, features closer to the centre (δ) correspond

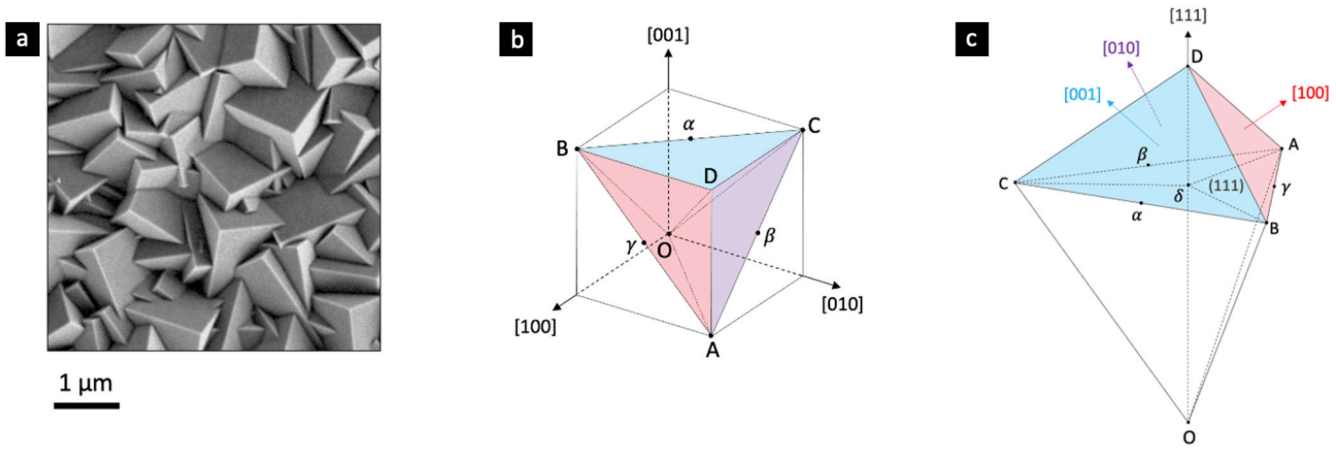

Fig. 1. Morphology of CVD (Ti,Al)N grains. (a) Plan view SEM micrograph of the (Ti,Al)N coating. (b) and (c) are 3D schematics of the Q-H pyramid illustrating the (001), (010) and (100) facets.

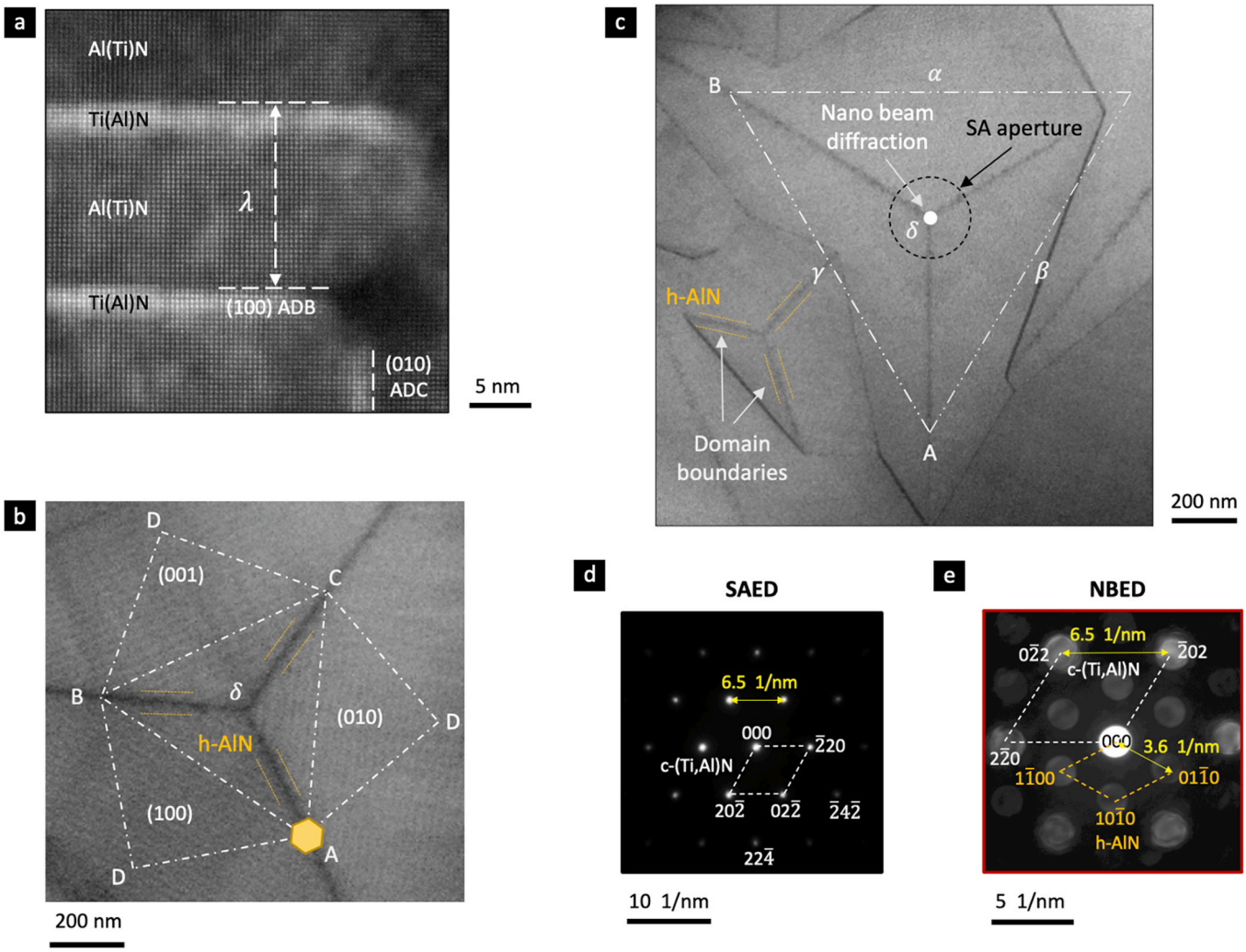

Fig. 2. Microstructure of CVD (Ti,Al)N grains. (a) Cross-sectional STEM HAADF micrograph viewed along the [001] zone axis, showing the internal nanolamella structure within the (Ti,Al)N grain. (b and c) Plan-view STEM HAADF micrographs view along the [111] zone axis, labelled with an unfolded Q-H pyramid, demonstrating the location of co-grown h-AlN at domain boundaries. (d) SAED pattern from the [111] zone axis. Location of the SA aperture is indicated in (c) by dashed circle in black. (e) NBED pattern from the [111] zone axis, obtained from the plan view section centre δ, as indicated in (c). Distance between 000 and $\bar{2}$ 20 reflection of the c-(Ti,Al)N phase is marked as approximately 6.5 1/nm in (d) and (e). Distance between 000 and 01 $\bar{1}$ 0 reflection of the h-AlN phase is marked as approximately 3.6 1/nm in (e).

to earlier growth stage, while those at the periphery form later, indicating that the epitaxial growth of {001} facets proceeds radially outward from δ towards the perphery of the plan view section.

Precipitates of wurtzite AlN (h-AlN) are observed at the {001}-faceted domain boundaries, especially at a location where Ti(Al)N sublayers from adjacent domains meet, as shown in Fig. 2 (b) and (c). Plan view sectional STEM imaging confirms that h-AlN is distributed along the boundaries (lines δA, δB and δC) between neighboring faceted domains. An unfolded Q-H pyramid demonstrates that δA corresponds to the projection of edge AD onto the (111) plane, while DA itself is shared by facets ADB and ADC as shown in Fig. 1 (b) and (c). Similarly, δB and δC are projections of edges DB and DC, respectively. The crystallographic orientation relationship between the (Ti,Al)N and domain boundary h-AlN is studied using electron diffraction from the plan-view section (tilted to [111] zone axis). In a SAED pattern, as shown in Fig. 2 (d), acquired with a selected area (SA) aperture position around δ (indicated in Fig. 2 (c)), only reflections from the cubic (Ti,Al)N phase are visible and diffraction spots of the h-AlN phase are too weak to be observed in a standard SAED pattern. The absence of the h-AlN reflection is attributed to the relatively small volume fraction of h-AlN compared to (Ti,Al)N, given the large aperture diameter (over 200 nm) used in SAED. However, NBED pattern acquired by placing a focused electron probe at δ successfully detects diffraction from both (Ti,Al)N and h-AlN. Identical NBED patterns are obtained when positioning the electron probe at other locations on lines δA, δB and δC, indicating that all h-AlN precipitates at {001}-faceted domain boundaries share a consistent crystallographic orientation relative to the (Ti,Al)N matrix. By indexing the NBED pattern in Fig. 2 (e), the orientation relationship between the cubic (Ti,Al)N and the domain boundary h-AlN phase is determined as:

$(11\ \bar{2})_{(Ti,Al)N}$ // $(10\ \bar{1}\ 0)_{AlN}$ and $[111]_{(Ti,Al)N}$ // $[0001]_{AlN}$

This relationship indicates that the (0001) basal plane of h-AlN aligns with the (111) plane of (Ti,Al)N, while the closed packed directions of h-AlN phase, i.e., [2 $\bar{1}\bar{1}$ 0], [$\bar{1}\bar{1}$ 20] and [$\bar{1}2\bar{1}$ 0], are parallel to the closed packed directions of (Ti,Al)N, i.e., [10 $\bar{1}$] (CA), [0 $\bar{1}$ 1] (AB) and [$\bar{1}$ 10] (BC), respectively.

A schematic describing the growth of (Ti,Al)N grain and the h-AlN precipitates on the domain boundaries is shown in Fig. 3. Fig. 3 (a) is an unfolded Q-H pyramid, aligning the {001} facets parallel to the (111) plane and indicating the ⟨001⟩, ⟨011⟩ and ⟨112⟩ crystal directions, providing a clearer view of the spatial arrangement of the faceted domains. This model is essential for understanding the 3D crystal rotation of the (Ti,Al)N grains.

The consistent crystallographic orientation of domain boundary h-AlN with respect to the (Ti,Al)N matrix suggests that the formation of h-AlN at domain boundaries is not random but is instead governed by epitaxial constraints imposed by the underlying (Ti,Al)N grain structure. The implications of this relationship, particularly regarding its potential role in influencing dislocation formation and crystal rotation, are further explored in Section 3.4.

Additionally, it should be noted that h-AlN also forms at the grain boundaries between adjacent (Ti,Al)N grains, as shown in Fig. 2 (c), and this type of co-grown h-AlN has been reported in a previous study [26]. Nevertheless, the faceted type of domain boundary h-AlN observed in this work has not been reported before. This is primarily because this layer of h-AlN is difficult to detect by conventional cross-sectional TEM analysis, and is only clearly visible with plan-view sectional TEM imaging employed in this study. Due to the TEM projection effect and limited dimension of the domain boundary h-AlN precipitates, it is difficult to determine exactly their size, although an estimated size less than 5 nm can be assumed.

3.2. Intra-grain misorientation of (Ti,Al)N

Detailed quantitative EBSD analysis was performed on sample 1 (λ = 15 nm) because its pronounced misorientation gradients provide the clearest insight into the crystal rotation phenomenon during growth. In subsequent sections, more concise EBSD analyses of samples 2 (λ = 35

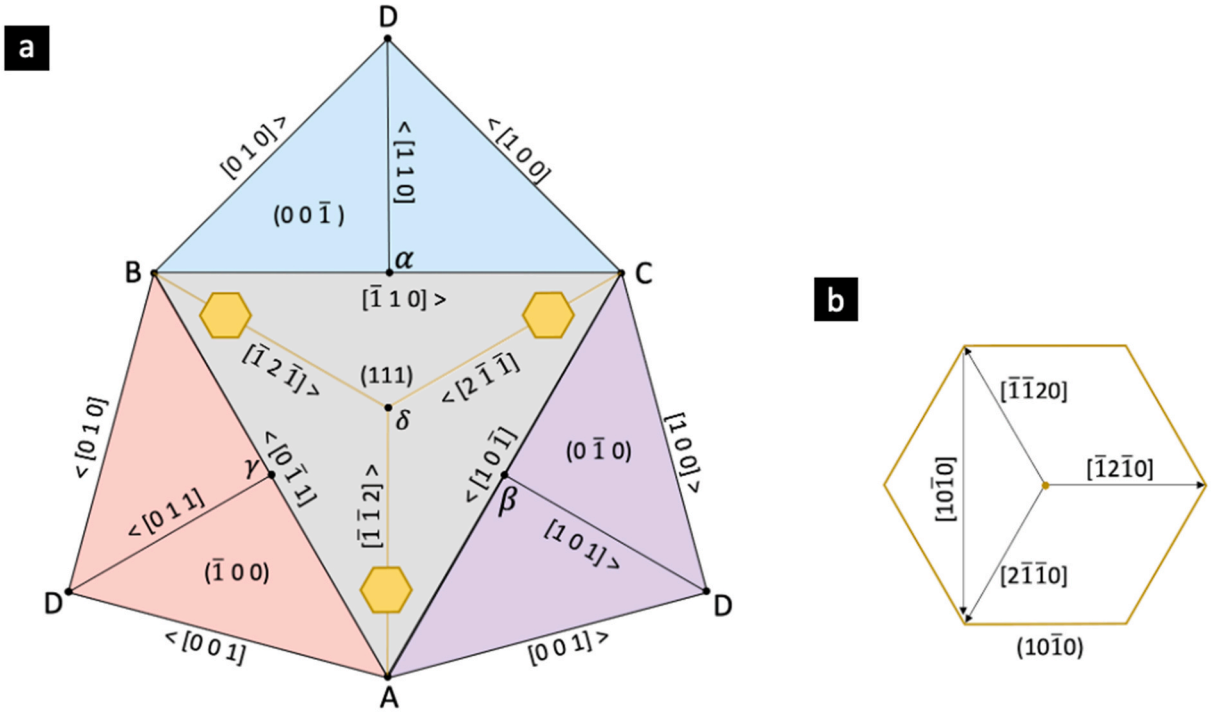

Fig. 3. Crystallographic orientation relationship between the (Ti,Al)N grain and domain boundary h-AlN precipitates. (a) Unfolded Q-H pyramid illustrating the three {001}-faceted domains and highlighting the domain boundary h-AlN, represented by hexagons corresponding to its basal plane. (b) Schematic hexagon representing the crystal orientations on the (0001) basal plane of domain boundary h-AlN.

nm) and 3 (without nanolamellae) are presented to demonstrate the influence of the internal nanolamella structure on the grain rotation.

Fig. 4 (a) presents a cross-sectional EBSD grain reference orientation deviation (GROD) map of the CVD (Ti,Al)N coating (sample 1, λ = 15 nm), in which the misorientation of individual pixels relative to the mean orientation of each grain is displayed. In almost all grains, a noticeable variation of GROD values can be identified. In each grain, the GROD value is around 0° in the middle of the grain and gradually reaches a maximum of up to 10° towards its bottom and top. The kernel average misorientation (KAM) map shown in Fig. 4 (b) shows that the misorientation between neighbouring pixels within the same grain is low and constant. No low-angle grain boundary, across which the crystal orientation changes abruptly, could be identified. These observations confirm that the crystal orientation undergoes a continuous change during growth.

Fig. 5 further illustrates this crystal rotation phenomenon. In Fig. 5 (a), a misorientation map of a typical columnar (Ti,Al)N grain (approximately 1 – 2 μm in width and 10 – 15 μm in height) shows a clear transition from blue at the bottom to red at the top, showing the gradual change in misorientation. A vertical misorientation angle profile in Fig. 5 (b), along the centre of the grain reveals a nearly linear increase, with a gradient of approximately 1°/μm across the entire grain cross-section.

The inverse pole figure (IPF) map in Fig. 6 (a) shows the crystal orientation of the same grain. It confirms that the macroscopic growth direction of the grain (the [111] crystal direction) is nearly parallel to the coating normal, resulting in the grain color appearing close to the blue corner of the colour legend shown in Fig. 6 (b). However, a subtle color shift is observed from the bottom (blue) to the top of the grain (dark purple), suggesting a gradual reorientation during growth.

The rotation axis of the misorientation is analysed by studying detailed pole figure structures, validating that the observed misorientation is due to a systematic rotation of the crystal lattice. Fig. 6 (c) shows pole figures of the grain viewed along the horizontal (Z) direction. It is demonstrated that one of the ⟨011⟩ directions remains fixed, as evidenced by a distinct and isolated spot marked in the 011 pole figure, while the other reflections exhibit elongated curves that trace segments of circular arcs. This distribution shows that the crystal undergoes continuous rotation around a nearly horizontal ⟨011⟩ axis.

To further explain the rotation, the 011 pole figure is re-plotted with the ⟨011⟩ rotation axis centred, as shown in Fig. 7 (a). In this re-aligned coordinate system, the x-, y- and z-axes correspond to [$\bar{2}$ 11], [111] (the grain growth orientation), and [0 $\bar{1}$ 1] (the rotation axis), respectively. The enlarged view in Fig. 7 (c) shows that the rotation about the [0 $\bar{1}$ 1] axis is approximately 20° in total, while the perpendicular angular spread of the [0 $\bar{1}$ 1] reflection is within 2°, see Fig. 7 (b).

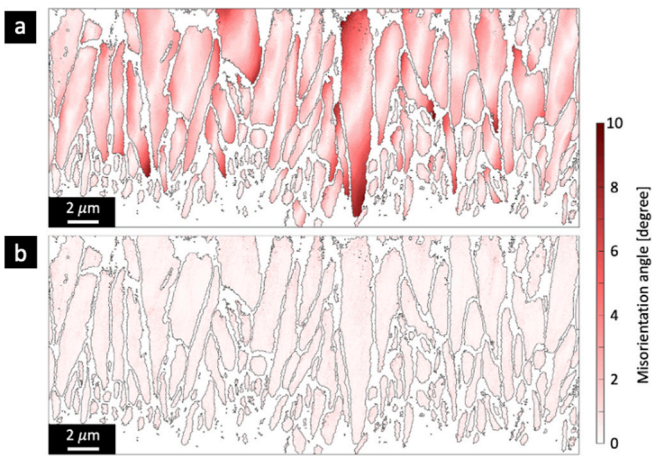

Fig. 4. Cross-sectional EBSD of the CVD (Ti,Al)N coating (sample 1, λ = 15 nm). (a) GROD map. (b) KAM map.

This type of crystal rotation is common feature observed consistently across all (Ti,Al)N grains examined by EBSD. For example, Fig. 8 shows cross-sectional EBSD maps of three additional grains (labelled as grains 1, 2 and 3). The rotation axes of these grains, as determined by pole figure analysis, exhibit different crystal orientations. Grain 1 has a rotation axis in the ⟨011⟩ family, similar to the grain in Fig. 7, while grains 2 and 3 display rotation axes in the ⟨112⟩ family. Overall, most grains show rotation axes that are nearly horizontal (parallel to the substrate surface) and perpendicular to the grain growth directions ([111] directions). The cause of this spread of horizontal rotation axes orientation is further analyzed in the following sections.

3.3. Plan view sectional EBSD analysis

Since vertical cross-sections (as in Figs. 4, 5, 6 and 8) intersect grains along arbitrary crystal planes, a randomness is introduced in the viewing direction. In addition, the intersection will be at random distances from the grain's central vertical axis. Thus, if the local misorientation varies not only vertically, but also laterally, this will affect the misorientation distribution of the grains in the cross-sectional EBSD map, and also lead to a variation of the observed crystal rotation axes.

To overcome this limitation, plan-view sectional EBSD is employed, where grains are sectioned parallel to the substrate. Given the strong 111 fiber texture of the (Ti,Al)N coating, the [111] direction of individual grains is nearly perpendicular to the substrate, meaning that the plan-view-section closely approximates the (111) plane. Thus, the plan-view-sectional EBSD enables direct visualization of rotation within the (111) plane, offering an additional analysis of the 3D crystal rotation behavior.

Fig. 9 (a) shows a misorientation angle map of a (Ti,Al)N grain on the plan-view-section. The misorientation angle systematically increases from the center towards the section periphery, reaching a maximum of 5° at the grain corners. The misorientation gradients along lines δA, δB and δC, which correspond to the edges of the pyramidal grain (AD, BD and CD in the Q-H pyramid) are shown in Fig. 9 (b), the gradients being around 4°/μm. In addition, Fig. 9 (c) presents the misorientation along lines AB, BC and CA, with gradients also around 4°/μm.

The directions of local crystal rotations on the same plan-view-section are also analyzed. Fig. 10 (a) is an IPF map along the coating growth direction (out of the paper). The colour of the IPF map is predominately blue (corresponding to the 111 corner in the color legend shown in Fig. 10 (e)), indicating that the [111] direction of the (Ti,Al)N grain is nearly parallel to the the subsrate normal, consistent with the strong 111 texture of the coating. However, a small variation in crystal orientation can be observed, particularly between the corners (corner A appears purple, while corners B and C exhibit a deeper blue). This color shift is consistent with the misorientation noted in Fig. 9 (a).

Fig. 10 (b) shows the pole figure of the {111} reflections, where the out-of-paper axis is aligned parallel to the [111] direction. The directions labelled δA, δB, δC, δα, δβ and δγ correspond to those in the plan-view-section shown in Fig. 10 (a). In the enlarged view of the vertical (111) reflections (marked by the dashed circle as [111] directions), a three-pointed star shape is visible, as shown in Fig. 10 (c). In the pole figure, pixels corresponding to points A, B, C, α, β, γ and δ in the plan-view-section are marked as P_A, P_B, P_C, P_α, P_β, P_γ and δ, respectively. Each corner of the star in the (111) reflection (P_A, P_B and P_C) relates to a specific corner in the plan-view-section (A, B and C) and thus with an edge of the pyramidal grain (AD, BD and CD). For a line, such as δA in the plan-view-section, the crystal orientation in the pole figure changes along an anti-parallel path, labelled δP_A. This alignment indicates that moving from the centre of the plan-view-section (δ) along the line δA in the plan-view-section corresponds to a gradual rotation of the [111] direction (normal to the (111) plane) towards the pyramid tip (D). This rotation occurs around an axis perpendicular to the line (δA) within the

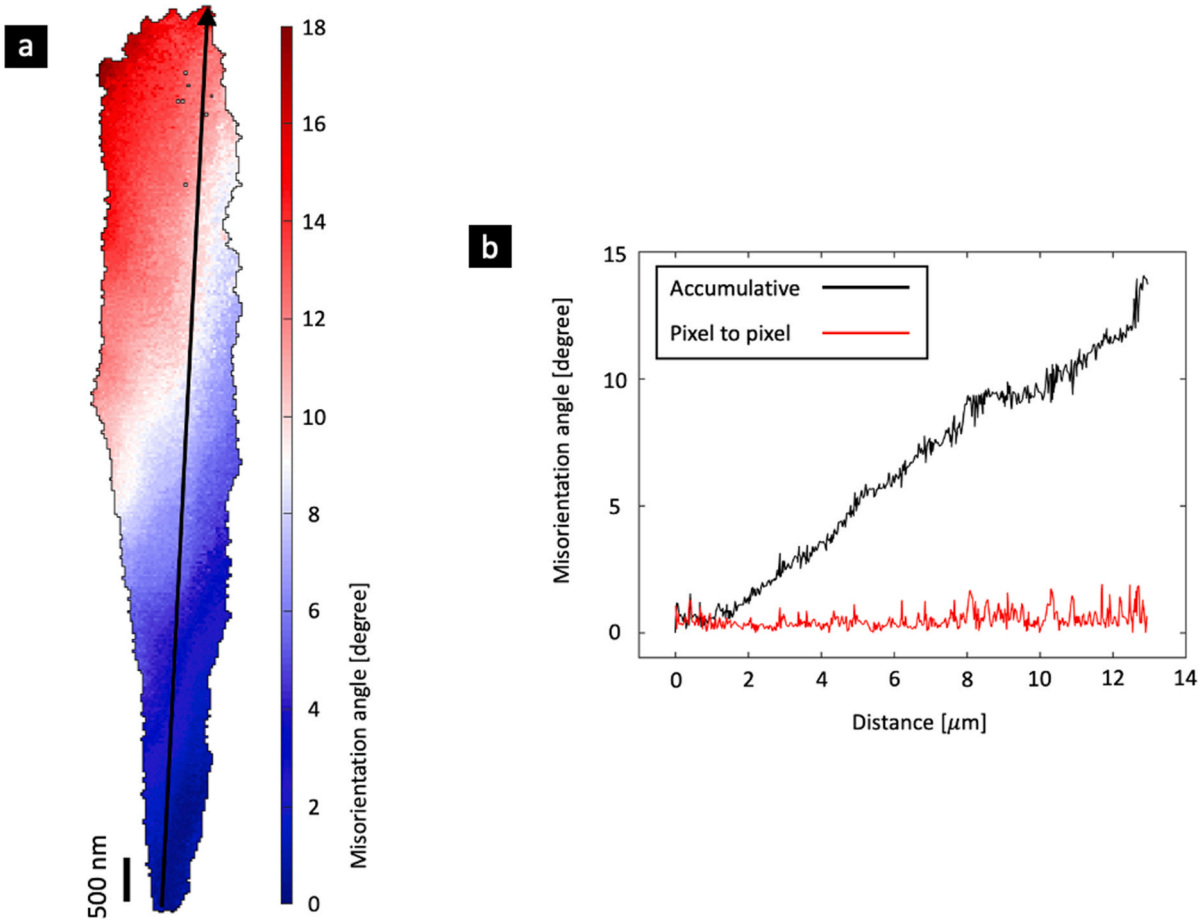

Fig. 5. Misorientation angle map and profile of a (Ti,Al)N grain (sample 1, λ = 15 nm) from cross-sectional EBSD. (a) Misorientation angle map showing the gradual increase in misorientation from the grain base to the top. (b) Misorientation along the line marked in (a), showing the cumulative misorientation angles relative to a reference pixel at the base (plotted in black), and the misorientation angle gradient relative to neighbouring pixels (plotted in red) along the same line. (For interpretation of the references to colour in this figure legend, the reader is referred to the web version of this article.)

(111) plane. Specifically, the rotation axis for line δA is BC. This pattern repeats for all lines extending from the centre (δ) to the periphery of the plan-view-section, including lines δB, δC, δα, δβ and δγ. Thus, the local grain rotation axis is always perpendicular to the grain growth direction [111].

In order to illustrate all the crystal rotation axes in the grain, Fig. 10 (d) shows a map of the local rotation axis for all pixels in the plan-view-section relative to the centre (δ). For misorientations along the lines δA (and δα), δB (and δβ) and δC (and δγ), the corresponding rotation axes are parallel to the lines BC, CA and AB, respectively. These axes align with the ⟨011⟩ directions, which are represented in green on the rotation axis map (refer to Fig. 10 (d)), according to the colour legend defined in Fig. 10 (e). Conversely, for misorientations along lines originating from δ and perpendicular to δA, δB and δC, the corresponding rotation axes are parallel to the lines δA, δB and δC, respectively. These axes align with the ⟨112⟩ directions, indicated in purple on the rotation axis map (see Fig. 10 (d)). Fig. 10 (f) shows the crystal rotation directions on the ABC (111) plane, along different lines originating from centre δ and pointing towards the periphery. The crystal rotation axes and directions are represented by a symbolic notation shown in Fig. 10 (g).

Additionally, the grain rotation along the lines in the plan-view-section is further illustrated in Figs. 11 and 12. Fig. 11 details the local crystal rotation along the line δB, marked by the red line in Fig. 11 (a). The crystal orientations for pixels only along line δB are plotted as a series of pole figures for the 001, 011, 111, 112, 134 and 145 reflections, as shown in Fig. 11 (b). These reflections in the pole figures form elongated curves that trace parts of circular trajectories around a common axis of crystal rotation [10 $\bar{1}$] (i.e., the CA direction), as indicated in Fig. 11 (a) and (b). The [10 $\bar{1}$] reflection in the 011 pole figure appears as a distinct spot, as this is the axis of crystal rotation.

Crystal rotations along any line in the (111) plane (i.e., the ABC plane), not just the line through the centre δ, will rotate along a perpendicular axis within this plane. As an example, illustrated in Fig. 12 (a), local crystal rotation along line CA has an axis along δB. This is confirmed by plotting pixels along the line CA in a series of pole figures shown in Fig. 12 (b), where elongated curves trace parts of circular trajectories around a common centre at the [$\bar{1}$ 2 $\bar{1}$] direction, which appears as a distinct spot in the 112 pole figure.

In summary, the peripheral regions of the pyramidal (Ti,Al)N grains bend outwards from the (111) plane towards the grain tip (D), as illustrated in Fig. 13. The crystal bends most at the pyramidal edges, specifically, at the boundaries between the three {001}-faceted domains (AD, BD and CD), corresponding to the corners of the plan-view-section ABC. The minimum crystal rotation, essentially zero, occurs along the central line of the grain, δD, which corresponds to point δ on the (111) section.

3.4. *Nanolamella structure and crystal rotation gradient*

To investigate the effect of the internal nanolamella structure within grains on the crystal rotation, plan-view-sectional EBSD analysis on three samples with varying nanolamella periodicities was conducted. A correlation between nanolamella periodicity and the crystal rotation gradient is shown in Fig. 12.

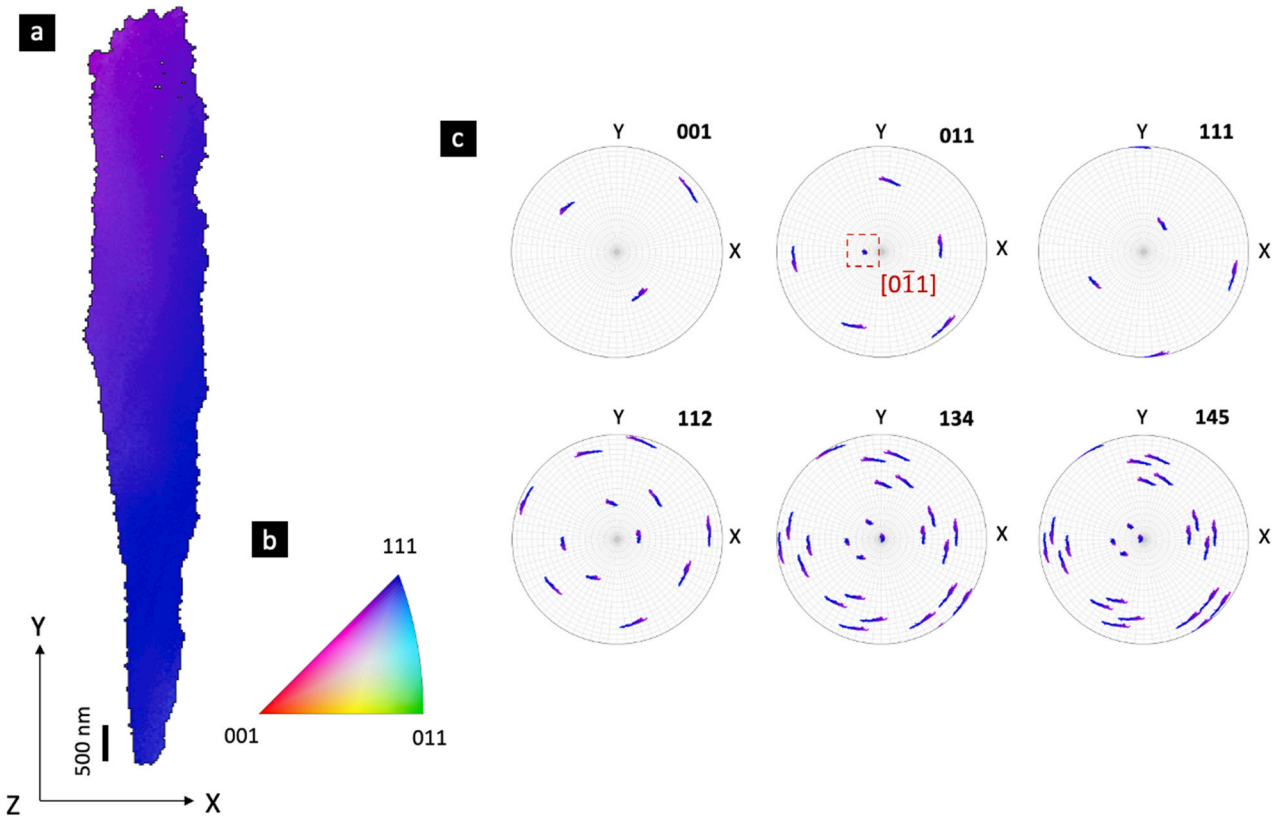

Fig. 6. Misorientation axis analysis of a (Ti,Al)N grain (sample 1, λ = 15 nm) from cross-sectional EBSD. (a) IPF map along the substrate normal direction (Y) for the same grain as in Fig. 5. (b) Corresponding color legend for the IPF map. (c) Pole figures (for 001, 011, 111, 112, 134 and 145 reflections) plotted in the specimen coordinate system (X-Y-Z), where Z is out of the paper, and Y is the coating normal direction (in the paper plane). The rotation axis along a direction belonging to the ⟨011⟩ family (specifically assigned as [0 $\bar{1}$ 1]) is indicated.

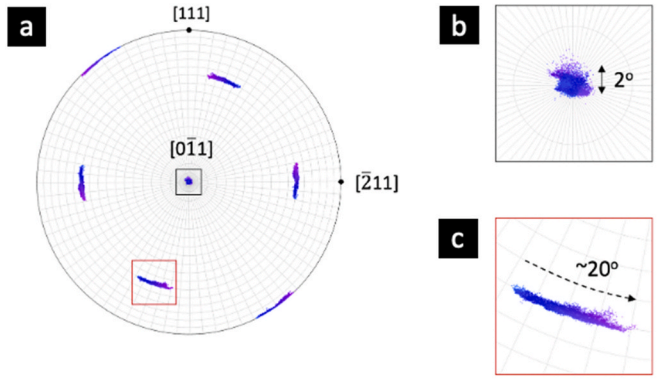

Fig. 7. Re-plotted 110 pole figure for direct measurements of the rotation angle. (a) The specimen coordinate system is re-aligned such that the y-axis corresponds to [111], the x-axis to [$\bar{2}$ 11], and z-axis to the rotation axis [0 $\bar{1}$ 1]. (b) An enlarged view of the [0 $\bar{1}$ 1] reflection. (c) An enlarged view of the [101] reflection.

Fig. 14 (a–c) present the misorientation angle maps for representative grains from sample 1 (λ = 15 nm), sample 2 (λ = 35 nm), and sample 3 (without nanolamella structure, i.e., λ = ∞). In all cases, the misorientation angle develops from the centre δ to the periphery, but with different gradients. As illustrated in Fig. 14 (d–f), the highest crystal rotation gradient is observed in sample 1 (3.4°/μm), close to that of the grain shown in Fig. 8, followed by sample 2 (1.9°/μm), while sample 3 exhibits the lowest gradient (0.6°/μm). Due to the low misorientation angle gradient and the limited lateral size of the grain in the plan-view-section, the misorientation between the periphery and the centre δ is almost undetectable on the EBSD map, see Fig. 14 (c).

3.5. *Reasons for the high internal grain rotations: High-density grown-in dislocations*

The classical Eshelby twist explains crystal rotation in 1D nanostructures, where a single axial dislocation with screw component causes continuous crystal rotation. However, this mechanism does not apply to our micron-sized 3D (Ti,Al)N grains, as the strain field of single dislocation is confined to only a few nanometers arounds it core. The substantial intra-grain rotation observed in this study must therefore originate from a collective strain field of numerous grown-in dislocations.

To better understand the microstructure of these (Ti,Al)N grains, a more detailed TEM analysis on three samples was conducted, as shown in Fig. 15. A noticeably high density of dislocations is observed inside the (Ti,Al)N grains in the cross-sectional STEM ADF images, shown in Fig. 15 (a–c). The dislocation density is so high in all three samples that individual dislocation lines are difficult to distinguish with standard TEM BF imaging. Therefore, diffraction contrast imaging in STEM mode, including ADF and BF imaging [29], was performed to observe these dislocations better.

The highest dislocation density is observed in sample 1 (λ = 15 nm), followed by sample 2 (λ = 35 nm), and the lowest dislocation density in sample 3 (without nanolamella structure, i.e., λ =∞). This means that the dislocation density increases with shorter nanolamella periodicity (more internal nanolamellae). Even with the enhanced spatial resolution of the STEM diffraction contrast imaging [29], individual dislocation lines in sample 1 cannot be clearly distinguished due to its exceptionally

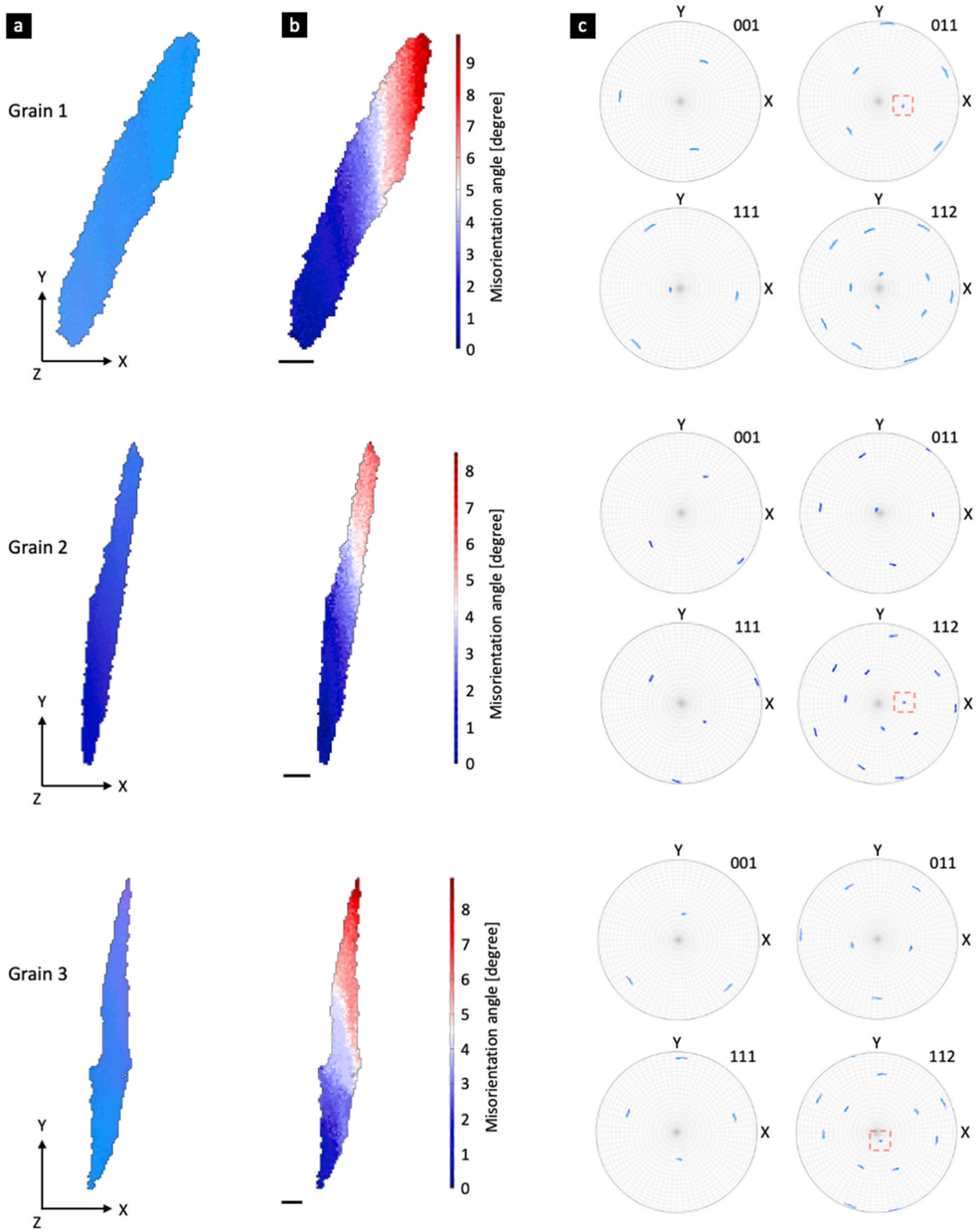

Fig. 8. Cross-sectional EBSD of three (Ti,Al)N grains (sample 1, $\lambda = 15$ nm). (a) IPF map along the coating growth direction (Y), color codes in Fig. 6 (b). (b) Misorientation angle maps. (c) Pole figures. Scale bars in (b) are 500 nm. Growth directions of all three grains are close to [111]. The rotation axes of grains 1, 2 and 3 are along crystal orientations belonging to ⟨011⟩, ⟨112⟩ and ⟨112⟩ families, respectively.

high dislocation density, see Fig. 15 (a). In contrast, individual dislocations are visible in the STEM ADF images of samples 2 and 3, as shown in Fig. 15 (b) and (c).

Within a {001}-faceted domain, dislocations originate at the boundaries with the neighbouring {001} domains (at the AδD, BδD, CδD planes), and extend as relatively straight lines almost along the epitaxial growth of the {001} planes. These dislocations are typical threading dislocations (TDs). In samples 1 and 2, TDs intersect with the nanolamellae on the {001} planes, as seen in the cross-sectional image shown in Fig. 15 (a) and (b). In sample 3 without the nanolamella structure, the

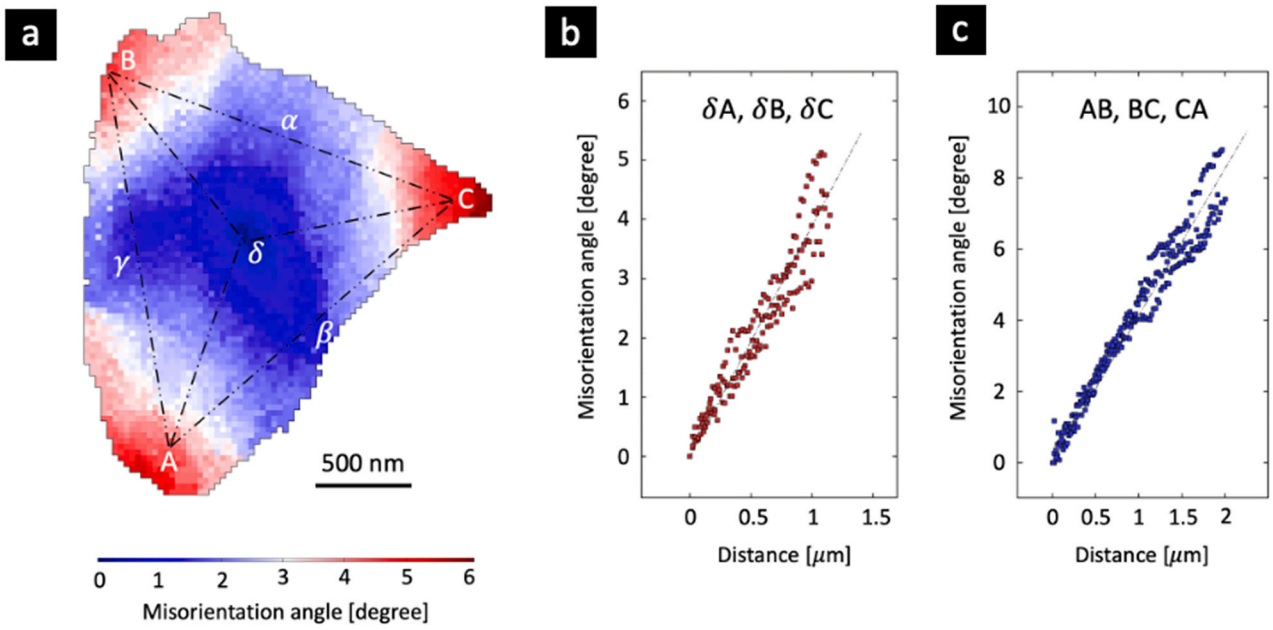

Fig. 9. Plan-view-sectional EBSD misorientation angles for a (Ti,Al)N grain. (a) Misorientation angle map with the reference pixel at the centre (δ) of the plan-view-section. Labels are given in the Q-H pyramid shown in Fig. 3. (b) Misorientation angle profiles along the δA, δB and δC directions. (c) Misorientation angle profiles along the AB, BC and CA directions.

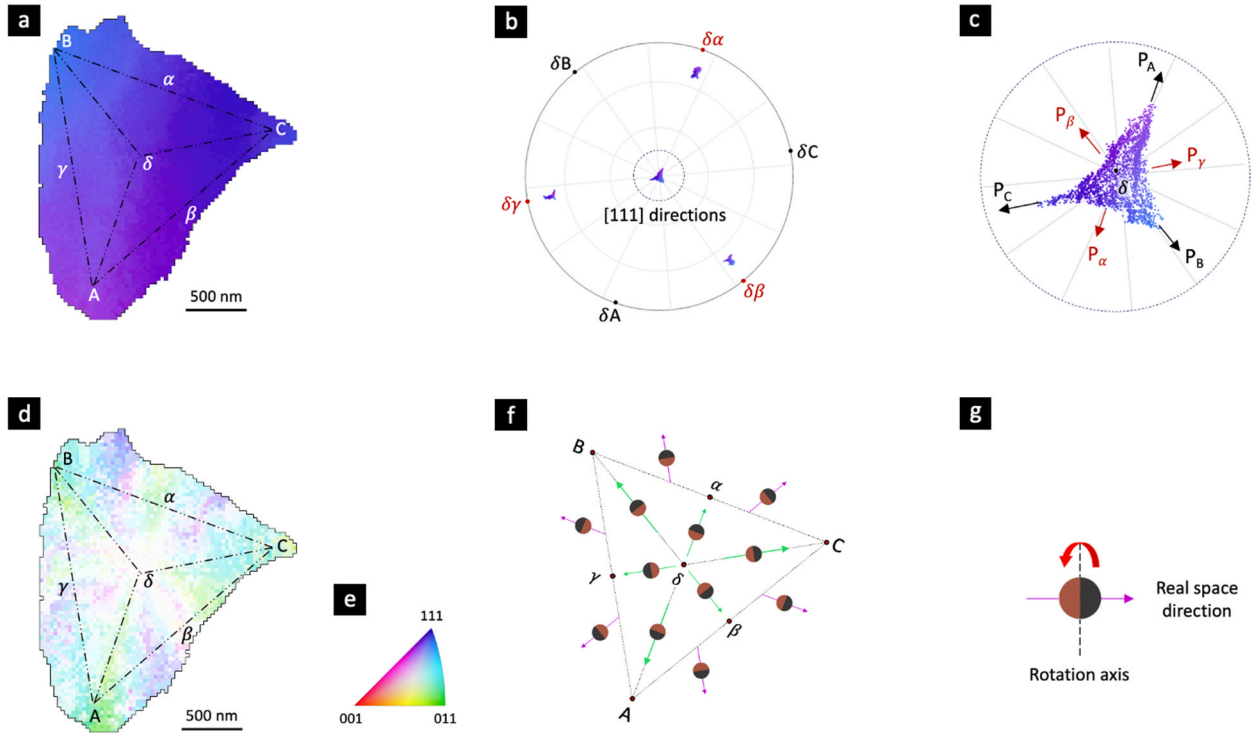

Fig. 10. Analysis of crystal rotation orientations by plan-view sectional EBSD. (a) IPF map along the coating growth direction (Y, pointing out of the paper). The grain is blue corresponding to a 111 growth direction, see legend in (e). (b) 111 pole figure, with the [111] direction pointing out of the paper (Y). The orientations of δA, δB and δC (in black), and δα, δβ and δγ (in red) are marked on the great circle of [111] (periphery of the pole figure). (c) Enlarged view of the central (111) reflection with key points (P_A, P_B, P_C, P_α, P_β, P_γ and δ) labelled, corresponding to the spots A, B, C, α, β, γ and δ in the Q-H pyramid, showing the overall variation of (111) due to the local crystal rotation. (d) Map of the rotation axis (colored according to (e)) derived from the EBSD data. (e) Color legend for crystallographic orientations. (f) Schematics showing the crystal rotation along different directions on the ABC (111) plane. (g) Notation showing the crystal rotation axis and direction. (For interpretation of the references to colour in this figure legend, the reader is referred to the web version of this article.)

TDs line orientations remain consistent with those in samples 1 and 2, suggesting that the nanolamella structure primarily influences dislocation density rather than their direction.

Plan-view STEM images for samples 1 and 3, as shown in Fig. 15 (d)

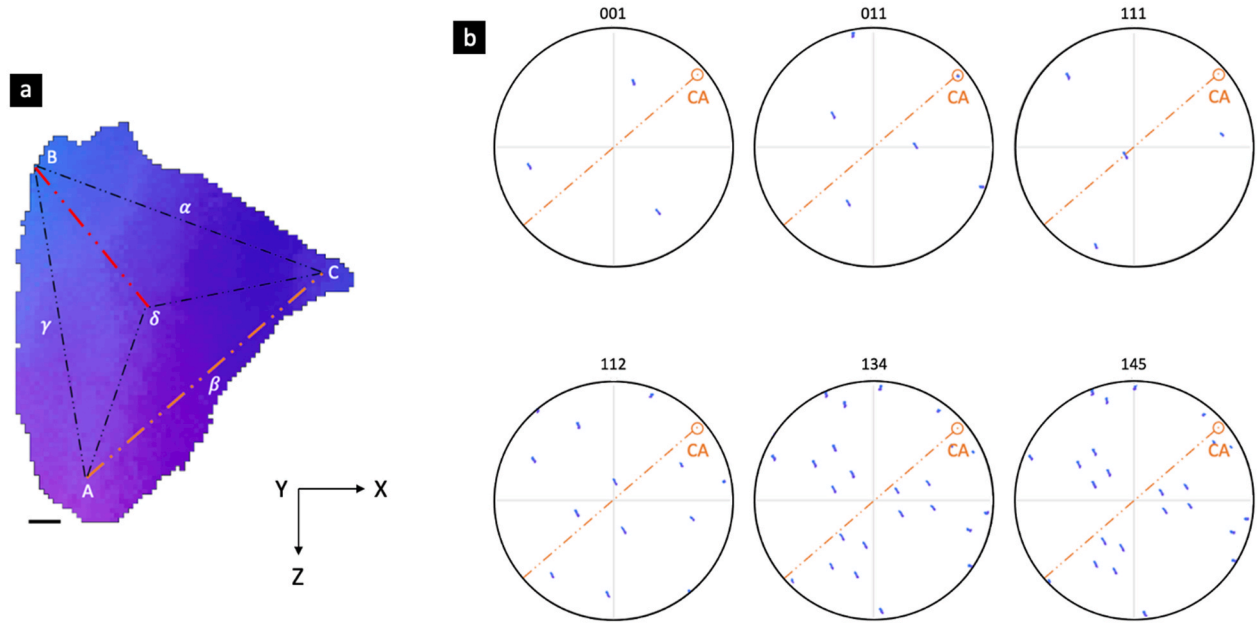

Fig. 11. Crystal rotations along line δ B (point-dashed line, red). (a) IPF map along the coating growth direction (Y), with specimen coordinates (X, Y and Z) indicated. (b) Pole figures for reflections 001, 011, 111, 112, 134 and 145 (only pixels along the line δB plotted), revealing that the rotation axis is parallel with CA (brown). Scale bar in (a) is 200 nm. (For interpretation of the references to colour in this figure legend, the reader is referred to the web version of this article.)

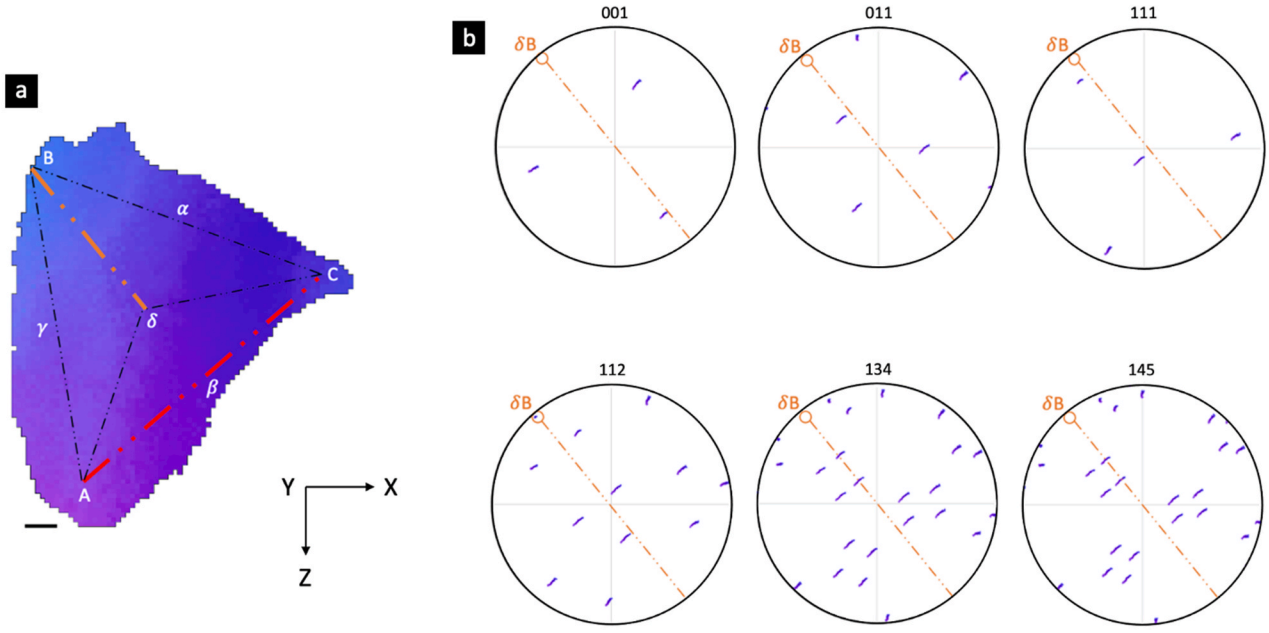

Fig. 12. Crystal rotations along line AC (red). (a) IPF map along the coating growth direction (Y), with specimen coordinates (X, Y and Z) indicated. (b) Pole figures for reflections 001, 011, 111, 112, 134 and 145 (only pixels along the line CA plotted), revealing that the rotation axis is aligned with δ B (brown). Scale bar in (a) is 200 nm. (For interpretation of the references to colour in this figure legend, the reader is referred to the web version of this article.)

and (e), further confirm that TD lines originate at the h-AlN/(Ti,Al)N domain boundaries and extend within each {001}-faceted domain along the growth direction (from the centre to the periphery of the section), in agreement with the cross-sectional observations.

It is reasonable to attribute the formation of these TDs to the lattice mismatch between the (Ti,Al)N and the co-grown h-AlN at the domain boundaries, as indicated in Fig. 15 (a) and (d). In addition, the TDs tend to align along specific directions within each domain, which reflects the crystallographic orientation relationship between the (Ti,Al)N grains and the h-AlN at the domain boundaries, as revealed in section 3.1. This will affect the TD line directions and Burgers vectors and will contribute to the crystal rotation for the (Ti,Al)N grains, as observed above.

Fig. 16 shows the proposed mechanism of the TD generation and subsequent crystal rotation of the (Ti,Al)N grain. As illustrated in Fig. 16 (a), the h-AlN nano-precipitate is believed to form at the boundaries between neighbouring {001}-faceted (Ti,Al)N domains. The lattice mismatch between h-AlN and (Ti,Al)N results in the TD formation. As shown in Fig. 16 (b), these TDs propagate in various directions along the epitaxial growth of {001} facets. The accumulation of TDs ultimately causes the (Ti,Al)N grain to rotate, as depicted in Fig. 16 (c). Fig. 16

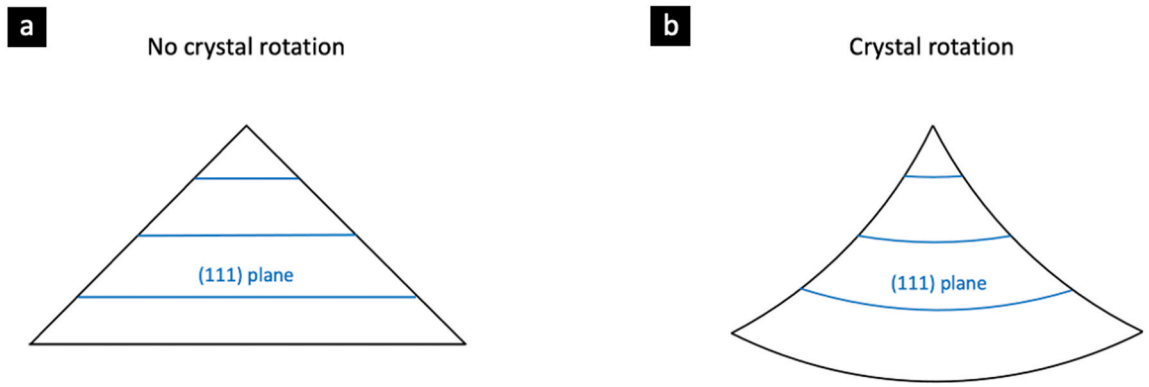

Fig. 13. Schematics of the crystal rotation in a pyramidal (Ti,Al)N grain, and its effect on the (111) planes. (a) No crystal rotation. (b) With crystal rotation.

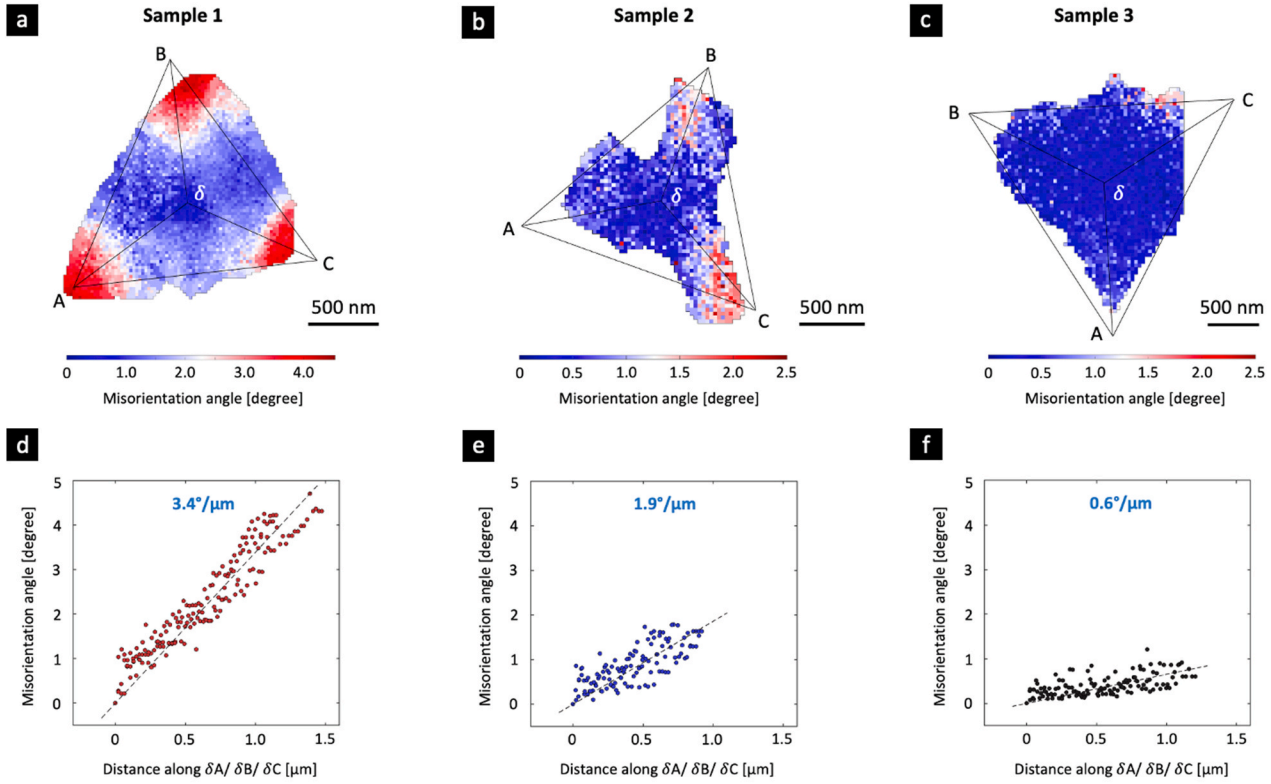

Fig. 14. Crystal rotation gradients for grains with different nanolamella structures. (a–c) Plan-view-sectional EBSD misorientation angle map for a representative grain from sample 1 ($\lambda = 15$ nm), sample 2 ($\lambda = 35$ nm), and sample 3 (without nanolamella structure, i.e., $\lambda = \infty$), respectively. (d–f) Misorientation angle as a function of distance along lines δA/δB/δC, for the grains shown in (a), (b) and (c), respectively.

shows the same crystal rotation phenomenon as displayed in Fig. 13, but from a different angle and in more detail.

The correlation between the crystal rotation gradients and the nanolamella periodicity can be attributed to the formation of domain boundary h-AlN and the resulting TD density. As shown in Fig. 2 (a), these h-AlN regions preferentially form at junctions shared by adjacent Ti-rich nanolamellae (Ti(Al)N) in neighbouring {001}-faceted domains. Consequently, (Ti,Al)N grains with a higher number of nanolamellae (i.e., a shorter periodicity, λ) contain more domain boundary h-AlN, leading to an increased density of the TDs and a greater crystal rotation.

The crystal rotation in the (Ti,Al)N grains should be linked to the TD line directions and their Burgers vectors, which should correlate with the crystallographic orientation relationship between the domain boundary h-AlN and the (Ti,Al)N grain. However, the details of this relationship are outside the scope of this study. To determine the 3D orientations of TD lines and their Burgers vectors, detailed trace analysis and two-beam diffraction experiments are necessary [30]. Additionally, further investigations into the lattice mismatch between (Ti,Al)N and domain boundary h-AlN, and its correlation with the dislocation Burgers vectors, could be systematically studied. Such studies are under way and will be published in a separate paper.

4. Conclusion

This study reports the first observation of an intra-grain crystal rotation phenomenon in CVD-grown (Ti,Al)N grains with a pyramidal morphology and internal nanolamella structures. The crystal rotation directions and gradients are systematically analyzed through cross-sectional and plan-view EBSD. Our finding reveals that the crystal rotation direction correlates with the 3D morphology of the (Ti,Al)N

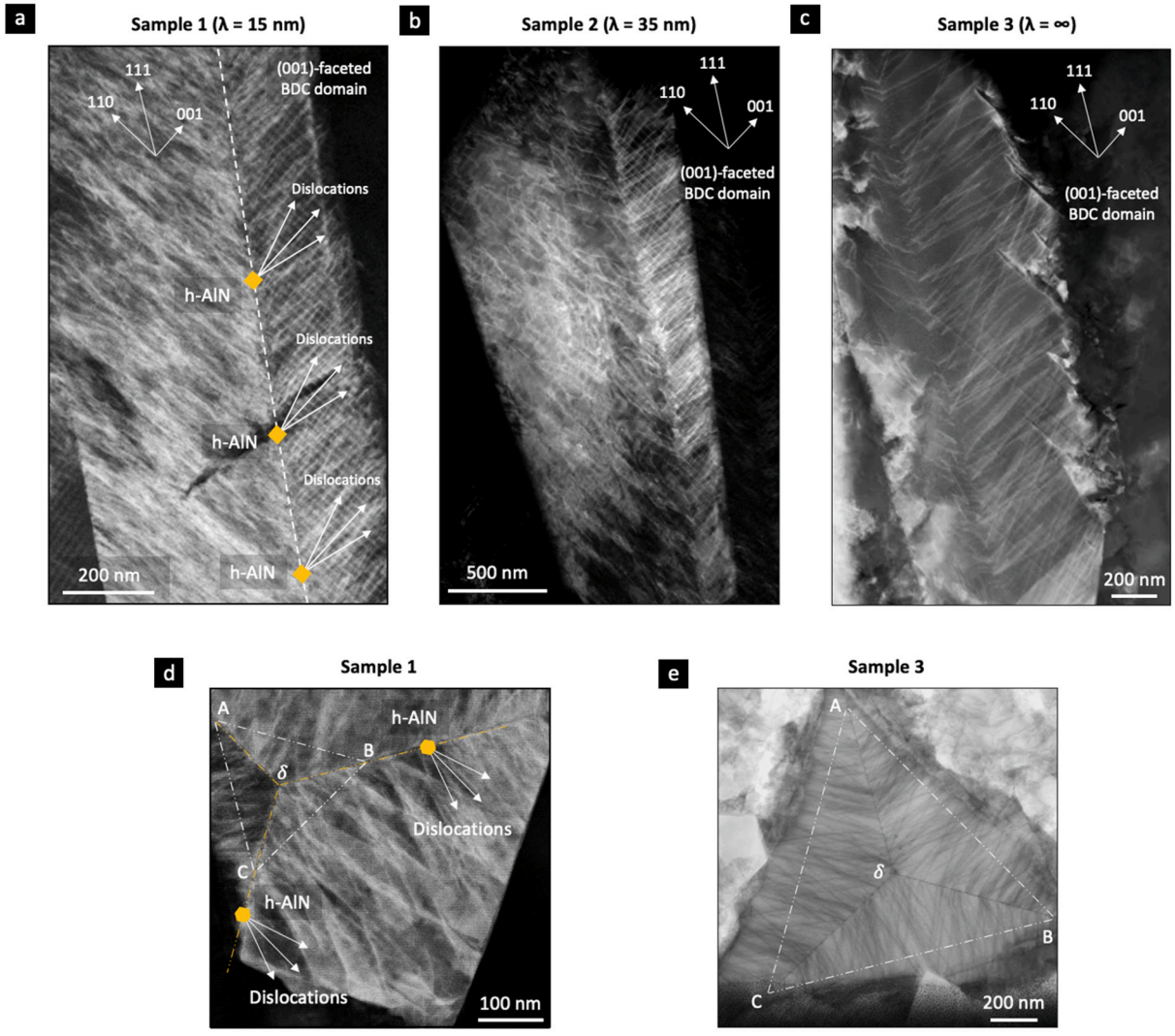

Fig. 15. Dislocations in (Ti,Al)N grains. (a–c) Cross-sectional STEM ADF micrograph collected from the [$\bar{1}$ 10] zone axis for sample 1 (λ = 15 nm), sample 2 (λ = 35 nm), and sample 3 (without a nanolamella structure, i.e., λ = ∞), respectively. (d) Plan-view-sectional STEM ADF micrograph collected from the [111] zone axis for sample 1. (e) Plan-view sectional STEM BF micrograph collected from the [111] zone axis for sample 3.

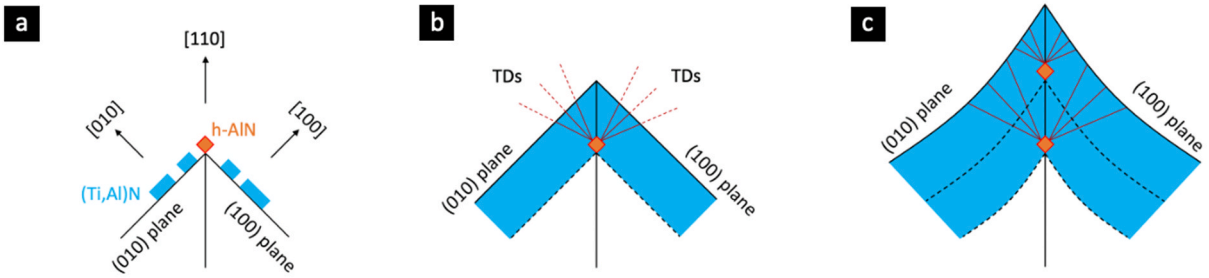

Fig. 16. Schematic illustrations of (Ti,Al)N grain rotation induced by co-grown domain boundary h-AlN and TD formation. The grains are viewed along the [1 $\bar{1}$ 0] axis. (a) Epitaxial growth of (Ti,Al)N {001} facets accompanied by the formation of h-AlN at the domain boundaries. (b) Generation of TDs due to lattice mismatch between the domain boundary h-AlN and (Ti,Al)N. (c) Crystal rotation due to high density of TDs.

grains, bending from the peripheral regions towards the grain tip. The rotation axes are consistently perpendicular to the grain growth direction along [111]. The rotation angle gradient in the vertical direction (from the base to the tip of the grain) is close to 1°/μm. The maximum rotation angle gradient in the horizontal directions is 3–4°/μm, near the pyramid edges. The crystal rotation is attributed to a high density of TDs that originate from the interface between the (Ti,Al)N grain and the co-grown h-AlN phase. The h-AlN phase forms at the boundaries of adjacent {100}-faceted (Ti,Al)N domains, and the crystallographic orientation relationships are revealed by electron diffraction analysis. Our findings reveal a previously unrecognized mechanism of grain growth and microstructural evolution in polycrystalline coatings during a CVD

process. Understanding this phenomenon of local grain rotations provides further insights into coating properties, for example, locally varying mechanical responses during external loading.

Declaration of Generative AI and AI-assisted technologies in the writing process

During the preparation of this work the authors used ChatGPT in order to improve language. After using this tool, the authors reviewed and edited the content as needed and take full responsibility for the content of the publication.

CRediT authorship contribution statement

Ren Qiu: Writing – review & editing, Writing – original draft, Visualization, Investigation, Formal analysis. **Olof Bäcke:** Writing – review & editing, Validation, Investigation. **Dirk Stiens:** Writing – review & editing, Validation, Investigation. **Hans-Olof Andrén:** Writing – review & editing, Validation. **Mats Halvarsson:** Writing – review & editing, Supervision, Project administration, Funding acquisition.

Declaration of competing interest

The authors declare that they have no known competing financial interests or personal relationships that could have appeared to influence the work reported in this paper.

Acknowledgements

Funding from "CVD 2.0", a Swedish Foundation for Strategic Research program via SSF contract RMA15-0048, is gratefully acknowledged. Dirk Stiens gratefully acknowledges support from the Swedish Foundation for Strategic Research by a strategic mobility grant (SM23-058). The analysis of materials microstructures was mainly carried out at the Chalmers Materials Analysis Laboratory (CMAL).

Data availability

Data will be made available on request.

References

[1] E.M. Trent, P.K. Wright, Metal cutting, Butterworth-Heinemann, 2000.
[2] A. van der Drift, Texture of a vapour-deposited lead-monoxide layer, Philips Res. Repts. 21 (1966) 289–303.
[3] A. van der Drift, Evolutional selection, a principle governing growth orientation in vapour deposition layers, Philips Res. Repts. 22 (1967) 267–288.
[4] S. Shoja, O. Alm, S. Norgren, H.-O. Andrén, M. Halvarsson, Calculated and experimental Schmid factors for chip flow deformation of textured CVD α-alumina coatings, Surf. Coatings Technol. 412 (2021) 126991.
[5] R. Qiu, S. Shoja, L. von Fieandt, J. Engqvist, O. Bäcke, H.-O. Andrén, M. Halvarsson, Schmid factors analysis for chip flow induced plastic deformation of textured coatings with rock salt structure, Int. J. Refract. Met. Hard Mater 108 (2022) 105932.
[6] S. Shoja, S. Norgren, H.-O. Andrén, O. Bäcke, M. Halvarsson, On the influence of varying the crystallographic texture of alumina CVD coatings on cutting performance in steel turning, Int. J. Mach. Tools Manuf 176 (2022) 103885.
[7] S. Shoja, O. Bäcke, A. Fazi, S. Norgren, H.-O. Andrén, M. Halvarsson, Enhanced steel machining performance using texture-controlled CVD alpha-alumina coatings: fundamental degradation mechanisms, Int. J. Mach. Tools Manuf 197 (2024) 104137.
[8] L. von Fieandt, K. Johansson, T. Larsson, M. Boman, E. Lindahl, On the growth, orientation and hardness of chemical vapor deposited Ti(C,N), Thin Solid Films 645 (2018) 19–26.
[9] L. von Fieandt, M. Fallqvist, T. Larsson, E. Lindahl, M. Boman, Tribological properties of highly oriented Ti(C,N) deposited by chemical vapor deposition, Tribol. Int. 119 (2018) 593–599.
[10] L. von Fieandt, T. Larsson, M. Boman, E. Lindahl, Texture formation in chemical vapor deposition of Ti(C,N), J. Cryst. Growth 508 (2019) 90–95.
[11] M. Ahlgren, H. Blomqvist, Influence of bias variation on residual stress and texture in TiAlN PVD coatings, Surf. Coatings Technol. 200 (2005) 157–160.
[12] A. Paseuth, K. Yamagata, A. Miura, M. Higuchi, K. Tadanaga, M. Cinibulk, Deposition and analysis of Al-Rich c-$Al_xTi_{1-x}N$ coating with preferred orientation, J. Am. Ceram. Soc. 100 (2016) 343–353.
[13] B.M. J., L.Y.K. Albert, K.A. V., S.A. L., J. Song, Dislocation-driven nanowire growth and Eshelby twist, Science (80-.) 320 (2008) 1060–1063.
[14] J. Zhu, H. Peng, A.F. Marshall, D.M. Barnett, W.D. Nix, Y. Cui, Formation of chiral branched nanowires by the Eshelby twist, Nat. Nanotechnol. 3 (2008) 477–481.
[15] S.A. Morin, S. Jin, Screw dislocation-driven epitaxial solution growth of ZnO nanowires seeded by dislocations in GaN substrates, Nano Lett. 10 (2010) 3459–3463.
[16] L.H.G. Tizei, A.J. Craven, L.F. Zagonel, M. Tencé, O. Stéphan, T. Chiaramonte, M. A. Cotta, D. Ugarte, Enhanced Eshelby twist on Thin Wurtzite InP nanowires and measurement of local crystal rotation, Phys. Rev. Lett. 107 (2011) 195503.
[17] P. Sutter, S. Wimer, E. Sutter, Chiral twisted van der Waals nanowires, Nature 570 (2019) 354–357.
[18] Y. Liu, J. Wang, S. Kim, H. Sun, F. Yang, Z. Fang, N. Tamura, R. Zhang, X. Song, J. Wen, B.Z. Xu, M. Wang, S. Lin, Q. Yu, K.B. Tom, Y. Deng, J. Turner, E. Chan, D. Jin, R.O. Ritchie, A.M. Minor, D.C. Chrzan, M.C. Scott, J. Yao, Helical van der Waals crystals with discretized Eshelby twist, Nature 570 (2019) 358–362.
[19] J.D. Eshelby, Screw dislocations in thin rods, J. Appl. Phys. 24 (1953) 176–179.
[20] M.S. A., B.M. J., T. Jonathan, J. Song, Mechanism and kinetics of spontaneous nanotube growth driven by screw dislocations, Science 328 (2010) 476–480.
[21] F. Ding, A.R. Harutyunyan, B.I. Yakobson, Dislocation theory of chirality-controlled nanotube growth, Proc. Natl. Acad. Sci. 106 (2009), 2506 LP – 2509.
[22] R. Qiu, O. Bäcke, D. Stiens, W. Janssen, J. Kümmel, T. Manns, H.-O. Andrén, M. Halvarsson, CVD TiAlN coatings with tunable nanolamella architectures, Surf. Coat. Technol. 413 (2021) 127076.
[23] D. Stiens, T. Manns, S. Ruppi, TiAlCN layers with lamellae structure, US patent 10,214,810 B2, 2019.
[24] R. Qiu, H. Aboulfadl, O. Bäcke, D. Stiens, H.-O. Andrén, M. Halvarsson, Atom probe tomography investigation of 3D nanoscale compositional variations in CVD TiAlN nanolamella coatings, Surf. Coatings Technol. 426 (2021) 127741.
[25] R. Qiu, L. von Fieandt, J. Engqvist, D. Stiens, O. Bäcke, H.-O. Andrén, M. Halvarsson, Facet identification in textured polycrystalline coatings by EBSD-aided SEM trace analysis, Mater Charact 209 (2024) 113743.
[26] R. Qiu, A. Forslund, O. Bäcke, A.H.S. Iyer, M. Sattari, W. Janssen, T. Manns, J. Kümmel, A. Ruban, D. Stiens, H.-O. Andrén, M. Halvarsson, Effects of gas flow on detailed microstructure inhomogeneities in LPCVD TiAlN nanolamella coatings, Materialia 9 (2020) 100546.
[27] F. Bachmann, R. Hielscher, H. Schaeben, Texture Analysis with MTEX – Free and Open Source Software Toolbox, Solid State Phenom. 160 (2010) 63–68.
[28] N. Thompson, Dislocation nodes in face-centred cubic lattice, Proc. Phys. Soc. B. 66 (1953) 481.
[29] P.J. Phillips, M.C. Brandes, M.J. Mills, M. De Graef, Diffraction contrast STEM of dislocations: Imaging and simulations, Ultramicroscopy 111 (2011) 1483–1487.
[30] D.B. Williams, C.B. Carter, Transmission Electron Microscopy: a Textbook for Materials Science, SpringerUS, Boston, MA, 2009.